Dynamic Stall Characteristics of Thick Wind Turbine Airfoils

Doosttalab, Mehdi; Ferreira, Carlos Simao; Ragni, Daniele; Yu, Wei; Rautmann, Christof

DOI
10.1002/we.70061

Publication date
2025

Document Version
Final published version

Published in
Wind Energy

Citation (APA)
Doosttalab, M., Ferreira, CS., Ragni, D., Yu, W., & Rautmann, C. (2025). Dynamic Stall Characteristics of Thick Wind Turbine Airfoils. *Wind Energy*, *28*(11), Article e70061. https://doi.org/10.1002/we.70061

Wind Energy

WILEY

RESEARCH ARTICLE OPEN ACCESS

Dynamic Stall Characteristics of Thick Wind Turbine Airfoils

Mehdi Doosttalab[1,2] | Carlos Simao Ferreira[2] | Daniele Ragni[2] | Wei Yu[2] | Christof Rautmann[1]

[1]Nordex Energy SE & Co. KG, Hamburg, Germany | [2]Faculty of Aerospace Engineering, Delft University of Technology, Delft, HS, the Netherlands

Correspondence: Mehdi Doosttalab (mdoosttalab@nordex-online.com)

Received: 15 May 2024 | **Revised:** 8 September 2025 | **Accepted:** 10 September 2025

Funding: This work was supported by the Nordex Energy SE & Co. KG.

Keywords: dynamic stall | flatback airfoil | wind tunnel | wind turbine

ABSTRACT

This paper studies the dynamic stall characteristics of thick flatback and nonflatback wind turbine airfoils. Two airfoils with a maximum thickness of 35% were studied, with trailing edge thicknesses of 2% and 10%, respectively. The static and dynamic experimental measurements were performed in the wind tunnel using surface pressure measurements for clean and tripped airfoils at the Reynolds number of $Re = 1 \times 10^6$ and dynamic reduced frequency ranging from 0.032 to 0.096. The effects of the trailing edge gap, roughness, mean angle of attack, and reduced frequency on the dynamic stall characteristics of the airfoils were investigated. The results show that increasing the trailing edge gap delays the onset of dynamic stall. However, the lift loss after the onset of dynamic stall is for the flatback airfoil higher than the sharp trailing edge airfoil. Moreover, the flatback airfoil show higher lift overshoot compared to the sharp trailing edge airfoil in the dynamic stall condition. Increasing the reduced frequency affects the dynamic behavior both airfoils differently.

1 | Introduction

Due to long-term uncertainty regarding the future price of oil, increased demand for energy, and environmental considerations, the wind energy industry has experienced rapid growth in recent decades [1]. Over the past three decades, there has been a significant increase in the size of newly developed wind turbines, with rotor diameters expanding from 10 to 15 m to a recent offshore turbine introduced by Vestas measuring 236 m in diameter. Design and development of such kinds of wind turbines have become a real challenge for designers, due to the lightweight and low-cost design considerations, while maintaining aerodynamic performance. This design evolution resulted in longer, more slender rotor blades, which carry more static and dynamic loads than the previous generation rotors.

On the other hand, this new design trend showed that increasing the thickness of the inboard-midspan section of the blade, especially the flatback airfoils, is one of the key techniques for improving structural and aerodynamic efficiency and reducing the blade weight [2, 3]. Furthermore, with increasing the rotor blade radius, the elasticity of the rotor blades is increased. Thus, the dynamic load's impact on the turbine will be increased [4]. These dynamic loads are usually related to wind gusts, rapid pitch angle change, yaw angle, wind shear, and aeroelastic torsion of the rotor blade due to the rotation.

Extremely unsteady flow conditions and a very complex three-dimensional flow field near the turbine are unfortunately not completely studied, among others [5–8]. The reduced frequency is used to categorize different unsteady flow regimes. Leishman [9] classified the unsteady flow conditions

for rotorcrafts into four categories. Steady flow for $k = 0$. For $0 \leq k \leq 0.05$ the flow is quasi-steady, and the unsteady effects are small, and they can be neglected. Unsteady flow can be considered from $k \geq 0.05$, and for $k \geq 0.2$ the flow is categorized as highly unsteady. Pereira et al. [10], on the other hand, suggested considering unsteady effects for $k > 0.02$ for wind energy applications. Leishman [9] classified the sources of unsteady aerodynamic loading on helicopter rotors into two periodic and aperiodic categories. Considering a wind turbine rotor, wind veer, atmospheric turbulence, wake inductions, and topological rotors are aperiodic sources of aerodynamic instabilities. On the other hand, yaw misalignment, blade–tower interaction, and wind shear are in the periodic unsteady aerodynamic category. As a result of these phenomena, the blades face different angles of attack, rotating from the top to the bottom of the rotor disc, which causes different loadings on the blades and thus different wake development, different inflow induction, and changing of the angle of attack.

Dynamic stall results from a rapid change of angle of attack on an airfoil, affecting the boundary layer on the surface of the airfoil so that the onset of stall occurs at several degrees higher than the standard static polar. Furthermore, it delays the flow reattachment process longer than the hysteresis effect, which happens at static lift polar. This phenomenon can lead to high loads on a wind turbine, which can damage the turbine or drastically reduce the fatigue life of the turbine. A sample of dynamic conditions for two different airfoils of a 117-m diameter Nordex turbine in two different wind turbulence conditions is shown in Table 1.

The characteristics of the dynamic stall effect have been observed and studied for many years [9]. One of the first researchers who observed this phenomenon is Kramer [11]. He addressed three primary phenomena that caused the delay in the stall onset. The first one is the unsteadiness in the circulation during increasing the angle of attack, which sheds into the wake and reduces the lift. The second relates to the virtual camber in a pitching airfoil, which decreases the leading edge pressure and pressure gradient on the suction side for a given lift coefficient. This effect was also observed by Ericsson [12], Carta [13], Johnson et al. [14], Ericsson et al. [15], McCroskey [16], and Beddoes [17]. The third one is related to the unsteady effects in the boundary layer, especially reversal flows in the presence of external pressure gradients. This has been observed by McAlister et al. [18], Scruggs et al. [19], Telionis [20], and McCroskey [21]. All the mentioned phenomena onset delay of stall. Ultimately, with a further increase in the angle of attack, a high adverse pressure gradient near the leading edge leads to flow separation. Leishman [9] addressed the formation of a free shear layer downstream of the leading edge, which rolls up quickly and forms vertical structures in the boundary layer that move towards the trailing edge and change the pressure distribution of the suction side in a favorable manner, which causes the increase of the lift. This vortex shedding process has been studied by Ham [22], McCroskey et al. [23, 24], and Beddoes [25]. Later, more experimental studies opened up a better understanding of the onset of dynamic stall [17, 26–28]. Liiva et al. [29] and Wood [30] performed a full-scale experiment to study the dynamic stall on helicopter rotor. The results showed that the dynamic stall quality is almost Mach number independent under different forcing conditions; however, the quantity behavior of dynamic stall could vary in different Mach numbers, different airfoils, and the presence of 3D conditions [9]. Figure 1 illustrates various stages of dynamic stall, which was calculated using the commercial CFD Fluent solver on an in-house airfoil with 18% relative thickness.

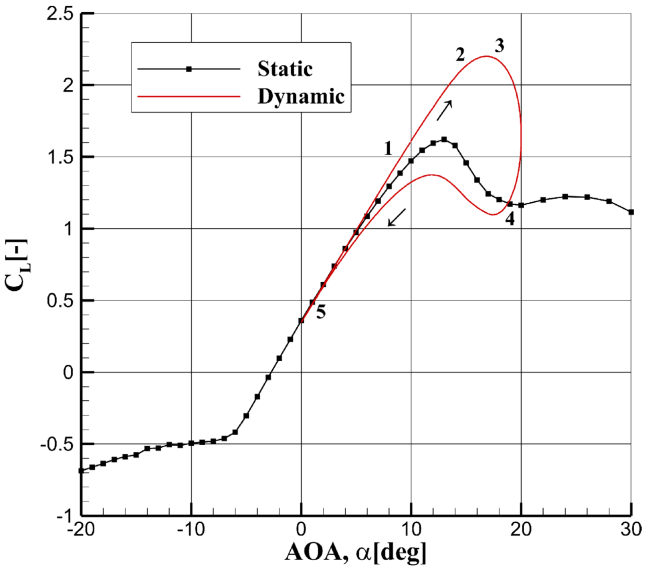

FIGURE 1 | Different stages of dynamic stall.

TABLE 1 | Dynamic stall boundary conditions for two airfoils of the N117 wind turbine.

Airfoil thickness		35%			30%		
Wind condition	Wind speed (m/s)	Mean AOA α_m(°)	Amplitude A (°)	Reduced fq k (–)	Mean AOA α_m(°)	Amplitude A (°)	Reduced fq k (–)
NTM	$V_{in}+2$	10	18	0.16	6	5	0.02
	V_r-2	14	19	0.15	7	5	0.02
	V_r	16	16	0.14	7	6	0.02
	V_r+2	17	17	0.13	5	8	0.02
	V_{out}	18	21	0.09	0	9	0.02
ETM	V_r	17	27	0.14	6	9	0.02
	V_{out}	20	29	0.09	0	10	0.02

The URANS two-equation $k-\omega$ *SST* turbulence model was utilized, along with the PISO algorithm, to simulate the dynamic stall phenomenon at a Reynolds number of $Re = 6 \times 10^6$. In Stage 1, the up-stroke phase, that is, increasing the angle of attack, on the linear part of the lift curve, the flow reversal appears in the boundary layer in the presence of the reduced adverse pressure gradient due to the kinematic pitch rate. The flow separation at the leading edge and the leading edge vortex formation occurs close to the end of the up-stroke phase or Stage 2. Moving this vortex on the suction side towards the trailing edge generates additional lift if it is close to the surface. For some low Mach number cases, it has been reported that this lift overshoot can reach up to 50% to 100% of maximum static lift coefficient [9]. However, this lift overshot can cause an abrupt nose-down pitching moment, which could be critical from the structural point of view. This is due to moving the suction peak along the suction side of the airfoil in conjunction with increasing the lever arm length. The speed of the moving vortex on the airfoil is estimated to be between one-third to half of the free stream velocity [31, 32]. In Stage 4, the vortex leaves the trailing edge and enters the wake downstream of the airfoil. At this moment, flow is fully separated on the suction side of the airfoil, and the flowfield is the same as the static flowfield at this attack angle. With decreasing the angle of attack, the reattachment process begins, however, with a considerable delay compared to the static lift polar [33]. This lag is related to the effect of reverse kinematic-induced camber due to a negative pitch rate on the leading edge pressure gradient. Stage 5 represents the fully attached flow situation. The mentioned hysteresis in different stages reduces the aerodynamic damping, potentially leading to aeroelastic problems on the rotor blade [9].

As mentioned above, modern long wind turbine blades employ thick airfoils up to the midspan of the blade to improve the blade weight and structural efficiency. Utilizing high relative thickness airfoils more towards the midspan section exposes them to higher dynamic loads and high angles of attack fluctuations. However, since these airfoils have a naturally low stall angle of attack, active or passive flow control methods are used to overcome this problem. Using blunt trailing edge airfoils [2] is one of the most advanced and effective solutions. These so-called flatback airfoils are generated by adding thickness over the camber line at the aft portion of the sharp trailing edge airfoils. Flatback airfoils have several structural and aerodynamic performance advantages compared to the conventional thick wind turbine airfoil with a sharp trailing edge. Due to the reduction of the adverse pressure gradient on the suction side of the thick trailing edge airfoil, a flatback airfoil has a higher lift coefficient and higher lift curve slope compared to the sharp trailing edge airfoil with the same thickness [2]. Furthermore, the lift coefficient of flatback airfoils has lower sensitivity to the leading edge soiling than the traditional sharp trailing edge airfoils, which is highly demanded in wind energy. Moreover, because of the increase in the trailing edge gap, these kinds of airfoils have a higher sectional area and sectional moment of inertia for a given airfoil maximum thickness [2, 3, 34].

1.1 | Objective

However, our current knowledge and understanding of the dynamic behavior of thick flatback airfoils, which is necessary for the load assessment, analysis, and certification of a wind turbine, is extremely limited. Lack of knowledge in this section could lead to enormous errors in the dynamic load calculations of rotor blades, which result in a poor design and, eventually, damage to wind turbines. This investigation aims to broaden the knowledge in this field and to investigate the effect of trailing edge thickness on the dynamic stall behavior of the high relative thickness wind turbine airfoils. Therefore, a wind tunnel campaign was planned to study the effect of trailing edge thickness on the dynamic stall characteristics of two thick airfoils. Several reduced frequencies and mean angles of attack in different parts of the lift curve, that is, linear part, prestall, stall, and poststall, were tested for both airfoils in the clean and tripped flow conditions.

2 | Experimental Setup

The experiments were conducted in the close return, Göttingen type, and low-speed low turbulence wind tunnel (LTT) of the Delft University of Technology [35]. The test section size is $1250 \times 1800 \times 2600$ mm with the nozzle contraction ratio 17.8: 1, which yields the turbulence intensity of 0.07% at a velocity of 75 m/s. The wind tunnel's maximum speed is 120 m/s at the empty test section. The wind tunnel is powered by a 525-kW variable-speed electric motor, which drives a six-bladed fan. To keep the air temperature inside the wind tunnel during the tests, a heat exchanger is installed in the settling chamber.

The aerodynamic tests were conducted on the X-35-02 and X-FB-35-10 airfoils at a Reynolds number of $Re = 1.0 \times 10^6$. These airfoils feature a maximum thickness of 35% located at 32% of the chord length, a leading edge radius of 5%, and trailing edge thicknesses of 2% and 10%, respectively. Additionally, both airfoils exhibit a maximum camber of 2.4% located at 78% of the chord length. Note that the second model is the flatback version of the former model with the same camber and relative thickness position. This flatback airfoil is constructed by adding gradual thickness around the camber line aft of the maximum relative thickness. The models have a chord length of 400 mm and a span of 1248 mm. They were milled from aluminum and mounted vertically in the wind tunnel's test section. The models are instrumented with 90 and 92 pressure taps, respectively. The

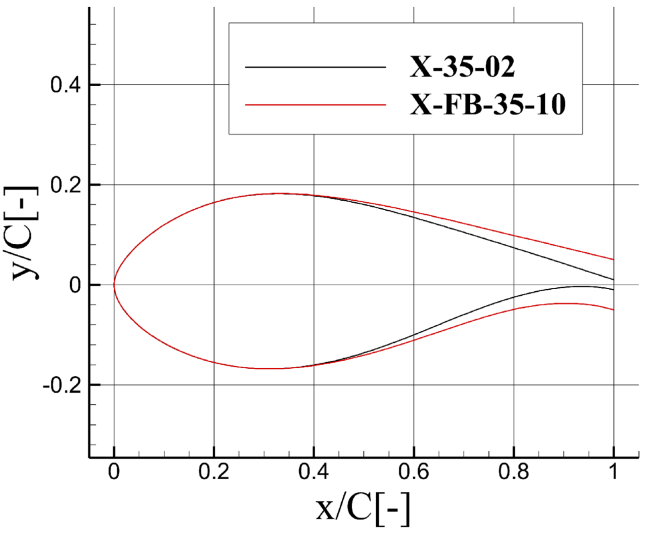

FIGURE 2 | Cross-sections of the X-35-02 and X-FB-35-10 airfoils.

pressure taps were installed on the model's surface with more density at the leading and trailing edges to resolve the high gradient areas. To simulate the leading edge contamination, trip zig-zag tapes with a thickness of 0.4 mm and width of 12 mm were mounted on the leading edge of the model at 5% and 10% of the chord position on the suction and pressure sides, respectively. The geometries of both airfoils are illustrated in Figure 2.

A highly accurate turntable was used to change the angle of attack of the airfoils in the wind tunnel for static measurements. However, a separate actuator mechanism was used to change the angle of attack during the dynamic tests. This mechanism is connected to a shaft located at the ¼ chord of the model and controlled digitally via a servomotor. This setup exerted a sinusoidal motion on the airfoil, and the mean angle of attack (α_m), amplitude (A), and frequency (fq) of the motion are adjustable. Using this setup, it is possible to pitch the airfoils with the frequency of 1–3 Hz, corresponding to the reduced frequency of 0.032, 0.064, and 0.096. This allowed for testing the airfoils under quasi-unsteady, unsteady, and highly unsteady conditions. The measurement of high pitch frequencies above 3 Hz was not achievable due to the limitations of the setup: including structural vibration of the model and overheating of the servomotor.

TABLE 2 | Test matrix of both airfoils in the steady conditions.

Airfoil	Reynolds no. (–)	Transition
X-35-02	1.00E+06	Free
X-35-02	1.00E+06	Forced
X-FB-35-10	1.00E+06	Free
X-FB-35-10	1.00E+06	Forced

A multichannel pressure data acquisition system was used to measure the static pressure on the surface of the airfoil and calculate the pressure (C_P), lift (C_L), and moment coefficients (C_M). The high-speed pressure scanner employed in this study samples all ports at a frequency of 300 Hz and is averaged for static measurements. Additionally, this sampling rate was utilized for the dynamic measurements, where data were collected for at least 20 cycles.

A traversed wake rake of 67 total pressure probes located downstream of the airfoil and connected to the data acquisition system was used to measure the drag. This method was used only for the X-35-02 airfoil in steady flow conditions. Since the measured drag coefficient using the wake rake leads to enormous errors for the separated flows [36], the integrated surface pressure measurements method was used to calculate the drag in the static and dynamic measurements of the X-FB-35-10 airfoil because of its naturally highly turbulent wake at the trailing edge. Moreover, the standard wind tunnel corrections, as given by Dalton [37], including the solid and wake blockage and streamline curvature, were applied to the measured data.

Due to the pressure tube length and the fluid characteristics, a method given by Bergh and Tijdeman [38] was used for phase and amplitude corrections of the dynamic pressure measurements, which is described in Appendix A. The corrected data were then used to calculate the aerodynamic coefficients of each airfoil. Finally, the conventional correction methods [37] were used to correct the aerodynamic coefficients. Note that the Dalton [37] method is not validated for the unsteady measurements.

A versatile test matrix was prepared to study different static and dynamic conditions on both airfoils, shown in Tables 2 and 3, respectively. Four static and 48 dynamic measurements

TABLE 3 | Test matrix of both airfoils in the dynamic conditions.

Airfoil	Reynolds no. (–)	Transition	Mean AOA α_m(°)	Amplitude A (°)	Frequency fq (Hz)	Reduced fq k (–)
X-35-02	1.00E+06	Free	6°	10°	1, 2, 3	0.032, 0.064, 0.096
X-35-02	1.00E+06	Free	10°	10°	1, 2, 3	0.032, 0.064, 0.096
X-35-02	1.00E+06	Free	STL-2°	10°	1, 2, 3	0.032, 0.064, 0.096
X-35-02	1.00E+06	Free	STL + 5°	5°	1, 2, 3	0.032, 0.064, 0.096
X-FB-35-10	1.00E+06	Free	6°	10°	1, 2, 3	0.032, 0.064, 0.096
X-FB-35-10	1.00E+06	Free	10°	10°	1, 2, 3	0.032, 0.064, 0.096
X-FB-35-10	1.00E+06	Free	STL-2°	10°	1, 2, 3	0.032, 0.064, 0.096
X-FB-35-10	1.00E+06	Free	STL + 5°	5°	1, 2, 3	0.032, 0.064, 0.096
X-35-02	1.00E+06	Forced	6°	10°	1, 2, 3	0.032, 0.064, 0.096
X-35-02	1.00E+06	Forced	10°	10°	1, 2, 3	0.032, 0.064, 0.096
X-35-02	1.00E+06	Forced	STL-2°	10°	1, 2, 3	0.032, 0.064, 0.096
X-35-02	1.00E+06	Forced	STL + 5°	5°	1, 2, 3	0.032, 0.064, 0.096
X-FB-35-10	1.00E+06	Forced	6°	10°	1, 2, 3	0.032, 0.064, 0.096
X-FB-35-10	1.00E+06	Forced	10°	10°	1, 2, 3	0.032, 0.064, 0.096
X-FB-35-10	1.00E+06	Forced	STL-2°	10°	1, 2, 3	0.032, 0.064, 0.096
X-FB-35-10	1.00E+06	Forced	STL + 5°	5°	1, 2, 3	0.032, 0.064, 0.096

were performed on both airfoils. Note that the mean angles of attack of 6° and 10° were fixed for both airfoils; however, the stall angle of attack of steady measurements was selected as a reference point and 2° and 5° before (*STL*-2°) and after (*STL*+5°) that were chosen as a mean angle of attack in the near stall conditions respectively. Furthermore, the amplitude of oscillations for prestall and poststall were 10° and 5°, respectively.

3 | Results

3.1 | Steady Conditions

Steady measurements were performed in free and forced transition flow conditions to have reference polars for the dynamic measurements and to see the performance difference between the normal and flatback version of the airfoil. Figure 3 shows the aerodynamic performance difference between X-35-02 and X-FB-35-10 airfoils in free and forced transition conditions. The results show that both airfoils have a high stall angle of attack in the free transition conditions. On the other hand, both airfoils perform very poorly in forced transition conditions, especially the X-35-02 airfoil. The stall angle of attack drops from 16° to 5°, and the stall on the pressure side starts at a 2° angle of attack. Furthermore, due to a heavy flow separation on both sides of the airfoil, a very low lift coefficient between these stall angles of attack is seen. These unfavorable characteristics are, however, expected due to the high-pressure gradient on both the pressure and suction sides of the airfoil, which is one of the main reasons for developing flatback airfoils. The effect of increasing the trailing edge thickness and therefore decreasing the pressure gradient on both airfoil sides can be seen on the polar of the X-FB-35-10 airfoil. With only increasing the trailing edge thickness aft of the maximum relative thickness, the lift coefficient was increased again to the free transition level, and the range between the pressure and suction side stall angle of attack increased rapidly. The drag polars show an increase of the drag in a wide range of angles of attack for the clean condition, comparing the X-35-02 to X-FB-35-10 airfoil. However, the drag of the flatback airfoil in the forced transition condition is lower than the X-35-02 airfoil in a wide range of angles of attack. This demonstrates that the excessive drag resulting from the increasing thickness of the trailing edge is less than the drag increase caused by the formation of separation bubbles on both sides of the airfoil.

Figure 4 shows the pressure coefficient comparison for the X-35-02 and X-FB-35-10 airfoils in free and forced transition flow regimes at different angles of attack. Note that the pressure discontinuity in the free transition flow regimes is related to forming the laminar separation bubble. The chord position of the laminar separation bubble, that is, the transition point, moves towards the leading edge with increasing the angle of attack. Furthermore, the effect of the zig-zag tape is visible in the pressure distribution on the suction side of the airfoil as a pressure leap downstream of the zig-zag tape.

Both airfoils show a solid performance in the free transition flow regime. Due to the reasonably low Reynolds number and high-pressure gradients on the surface of the airfoil, the laminar separation bubble transients the flow into turbulence. At low angles of attack, the flow remains attached to the surface of airfoils; however, with increasing the angle of attack to 15°, the trailing edge separation forms at the end part of the suction side of the X-35-02 airfoil but it is not extended enough to put the airfoil into stall. The lower pressure gradient of the X-FB-35-10 airfoil on its suction side is visible. With further increasing the angle of attack, trailing edge flow separation forms on both airfoils, which causes the stall. In the forced transition flow regime, the X-35-02 airfoil shows flow separation on the pressure side at 0° angle of attack. With increasing the angle of attack to 4°, flow separation forms at the trailing edge of the airfoil, and the flow becomes attached to the pressure side. The X-FB-35-10 airfoil, on the other hand, shows no sign of flow separation. As expected, with increasing the angle of attack, the flow separates on the suction side of both airfoils. Notice the big difference between the maximum suction

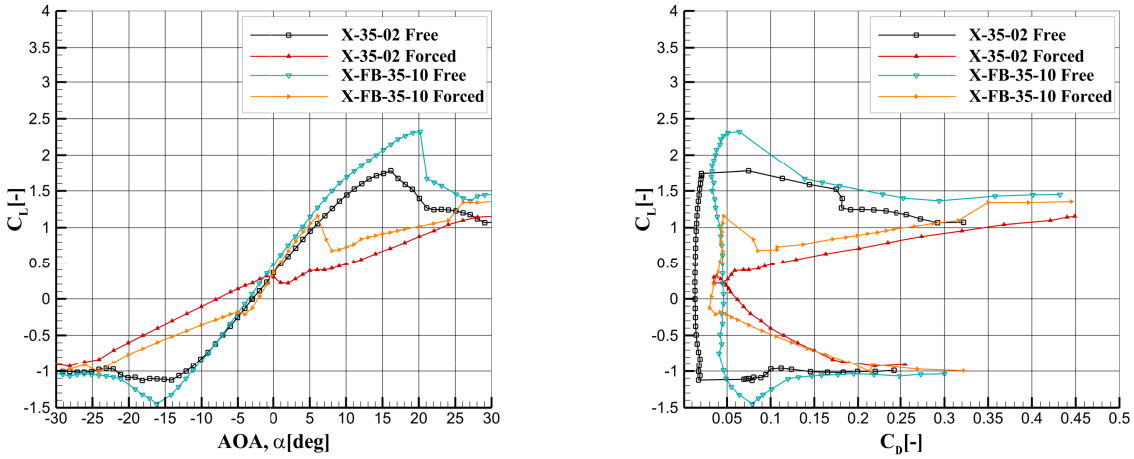

FIGURE 3 | Static free and forced transition polar curves for X-35-02 and X-FB-35-10 airfoils ($Re = 1 \times 10^6$).

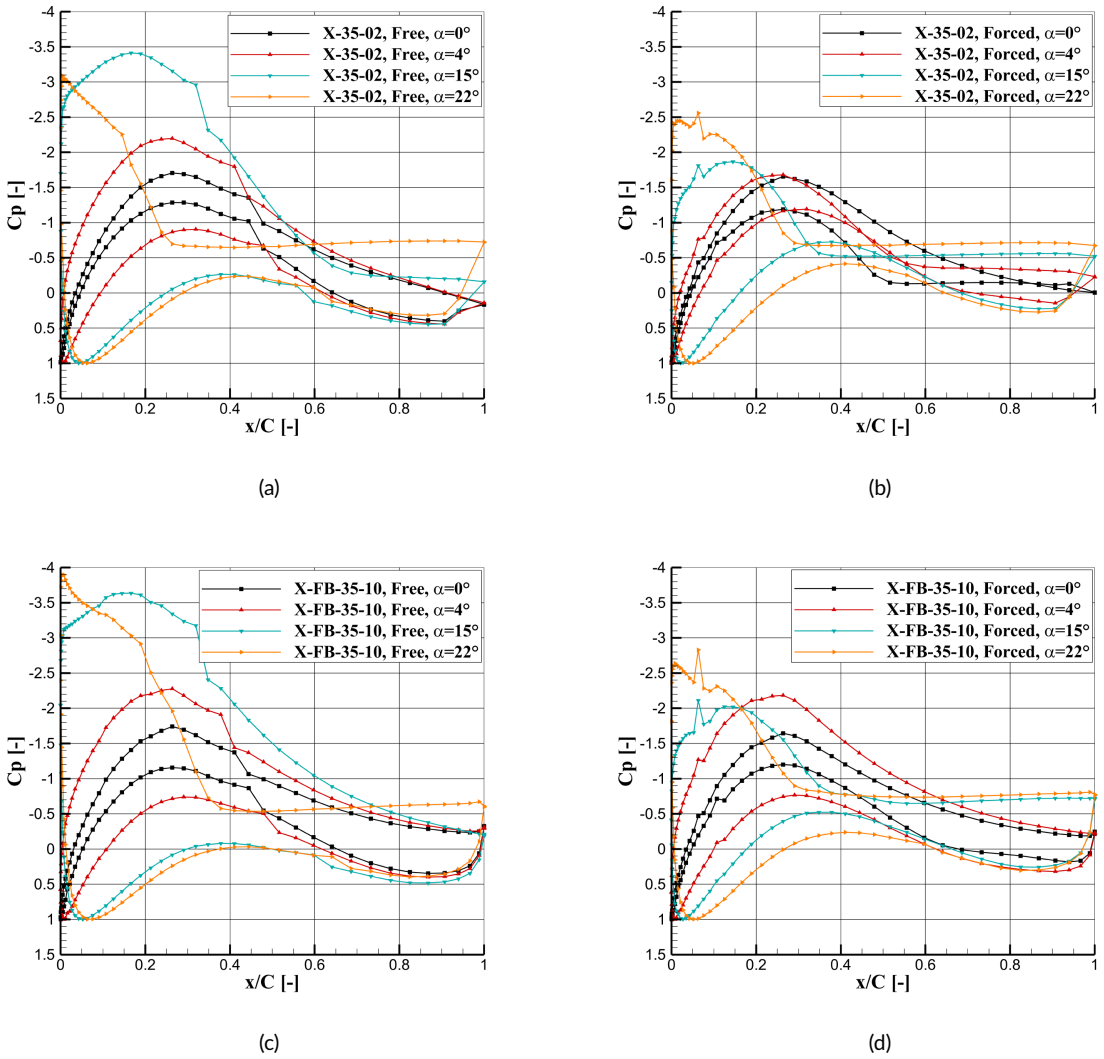

FIGURE 4 | Static pressure coefficient comparison for both airfoils, in free and forced transition flow regime ($Re = 1 \times 10^6$).

peak at high angles of attack between the free and forced transition flow regimes. The X-FB-35-10 airfoil shows slightly higher suction peaks in both free and forced transition flow regimes because of the lower pressure gradient aft of the maximum relative thickness.

The surface flow visualization of the X-35-02 airfoil at the angle of attack of 6° and $Re = 1 \times 10^6$ in the free transition flow regime is presented in Figure 5. The leading edge is on the left, and the trailing edge is on the right side of the picture. The laminar separation bubble formation is visible as a bright strip. After this region, the flow is turbulent. Note the running of the surface paint near the trailing edge, due to the gravity and lack of the flow momentum.

3.2 | Dynamic Conditions

Figure 6 presents the dynamic normal coefficient polars of X-35-02 and X-FB-35-10 airfoils in free and forced transition, at various mean angles of attack and a reduced frequency of $k = 0.064$. The DS-phases are represented by dash-dot-dot lines. Generally, when the flow remains attached to both airfoil surfaces during dynamic loops, the standard deviation of the normal force coefficients in the US-phase and/or DS-phase is low, resulting in clear footprint lines in the dynamic C_N polars. Conversely, the presence of separation bubbles on one or both sides of the airfoil leads to increased standard deviation of dynamic C_N values due to the unsteady behavior of the separation bubble. This results in noisy dynamic polars in at least one specific part of the loop.

Figure 6a shows the dynamic normal coefficients at the mean angle of attack of 6°. Both airfoils show a similar trend in the US-phase, where the C_N is lower than the static force due to the pressure adaptation lag of the flow to the new increasing angle of attack. Furthermore, the X-FB-35-10 airfoil demonstrates higher C_N values and a wider normal force range (NFR) compared to the X-35-02 airfoil, attributed to more favorable pressure gradient conditions above the airfoil. As the airfoils approach the top stagnation angle (TSA), trailing edge separation occurs on the suction side, although it is insufficient to induce stall. Consequently, the standard deviation of the dynamic C_N increases at the onset of the DS-phase, particularly for the X-35-02 airfoil due to its higher

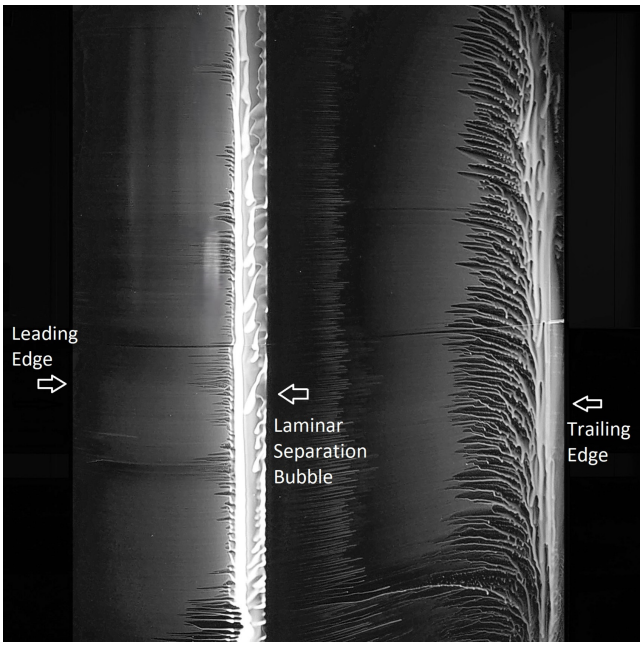

FIGURE 5 | Surface flow visualization on the suction side of the X-35-02 airfoil, in free transition condition ($Re = 1 \times 10^6$, $\alpha = 6^\circ$).

pressure gradients on the suction side and closer proximity to the static stall angle of attack compared to the X-FB-35-10 airfoil. The separation bubble grows rapidly under these flow conditions, leading to increased flow instabilities. These adverse conditions result in a reduction of the mean dynamic normal slope (MDNS) for the X-35-02 airfoil relative to the flatback airfoil. In the DS-phase, the C_N exceeds the stationary polar values due to the flow pattern adaptation lag. As the angle of attack decreases further, the separation bubble diminishes and disappears before reaching the bottom stagnation angle (BSA), promoting stable flow conditions. Consequently, the standard deviation of C_N decreases. The combination of pressure adaptation lag in the US- and DS-phases, without stall occurrence, generates counterclockwise oval loops.

By increasing the mean angle of attack to 10°, the X-35-02 airfoil surpasses the static stall angle of attack at the end of the US-phase, as depicted in Figure 6c. At the TSA, the pressure gradient on the suction side of the airfoil is so high that the trailing edge separation bubble bursts towards the leading edge. Unlike the previous cases ($\alpha_m = 6^\circ$), the C_N drops and the airfoil stalls dynamically. Note that the separation bubble becomes smaller and disappears as the angle of attack decreases. This can be detected by decreasing the standard deviation of the C_N at the end of the DS-phase. However, because of its extension and size, it remains longer above the airfoil than the lower mean angle of attack. Thus, the dynamic C_N slope remains low in a big portion of the DS-phase. Before the BSA, the flow is again fully attached and the dynamic C_N approaches the static value, due to decreasing the pitching rate ($d\alpha/dt$) and pressure adaptation lag close to the BSA. The US-phase begins again in fully attached condition, and the C_N remains below the static values as described before. Consequently, the dynamic loops are eight-shaped. On the other hand, the C_N cycle behavior of the X-FB-35-10 airfoil is now similar to the X-35-02 airfoil at the $\alpha_m = 6^\circ$ but with slightly more trailing edge flow separation at the TSA. Still, it is not extended enough to fully stall the airfoil and a slight decrease of the C_N is visible at the TSA. Again, because of more stable flow conditions, the X-FB-35-10 airfoil exhibits a wider NFR and higher MDNS compared to the other airfoil. It can be seen clearly that the flatback airfoil delays the onset of the dynamic stall compared to the X-35-02 airfoil, which results in higher C_N overshoots.

The dynamic results of the $\alpha_m = STL\text{-}2^\circ$ are depicted in Figure 6e. Here, because of the incident of the dynamic stall, both airfoils show the same eight-shape dynamic C_N loops. The X-FB-35-10 airfoil has a longer C_N US-phase than the other airfoil due to its more stable flow characteristics. On the other hand, the flatback airfoil has a more abrupt stall characteristic than the X-35-02 airfoil. A higher stall angle of attack generates higher pressure gradients on the suction side of the airfoil, which leads to a faster expansion of the separation bubble, compared to the X-35-02 airfoil. Furthermore, the minimum C_N in this scenario is lower than that at the end of the DS-phase, and the NFR value continues to be higher for the flatback airfoil. The X-35-02 airfoil exhibits a slightly higher MDNS than the flatback airfoil.

Figure 6b,d presents the forced transition dynamic polars of both airfoils at the mean angle of attack of 6° and 10°, respectively. As the mean angle of attack for the X-35-02 airfoil falls within the poststall region, heavy flow separation occurs above both the suction and pressure sides at the conclusion of the DS-phase. Consequently, the C_N cycles maintain a flat, oval shape. For the X-35-02 airfoil in both cases, the TSA and BSA are beyond the positive and negative stall angles of attack and the MDNS is very close to the static curve. However, the X-FB-35-10 airfoil shows a different behavior, that is, dynamic stall occurs for the both mean angles of attack. The reason is that the BSA is in the linear stable part of the static polar and the US-phase starts with the attached flow on the suction side of the airfoil. The flow starts to separate only at the end part of the US-phase, where the deviation of the dynamic C_N becomes visible. This large trailing edge separation bubble disappears at the BSA for the $\alpha_m = 6^\circ$ and $\alpha_m = 10^\circ$. Once more, the MDNS of the flatback airfoil remains significantly higher than the other airfoil. Therefore, the C_N overshoot values are much higher than the X-35-02 airfoil in forced transition conditions.

And finally, Figure 6f shows the dynamic stall behavior of both airfoils in poststall conditions. These oval loops contrast with the linear part of the polar, cycling clockwise. It is evident that the X-35-02 airfoil exhibits a smooth and steady stall compared to the abrupt stall of the flatback airfoil, where trailing edge separation gradually progresses towards the leading edge during stall onset. Consequently, at the onset of the US-phase of the X-35-02 airfoil, the trailing edge separation bubble is smaller than that of the flatback airfoil, resulting in dynamic normal force values approaching the maximum steady values. On the other hand, the X-FB-35-10 airfoil has a bigger separation bubble at the BSA compared to the X-35-02 airfoil. In deep stall conditions, the trailing edge vortex of the flatback airfoil combines with the suction side separation bubble and creates a multiple separation bubble zone. This separated zone is not affected efficiently by increasing the angle of attack. Therefore, the dynamic C_N deviates less for the flatback airfoil during the US-phase. This results in a higher NFR value for the X-35-02

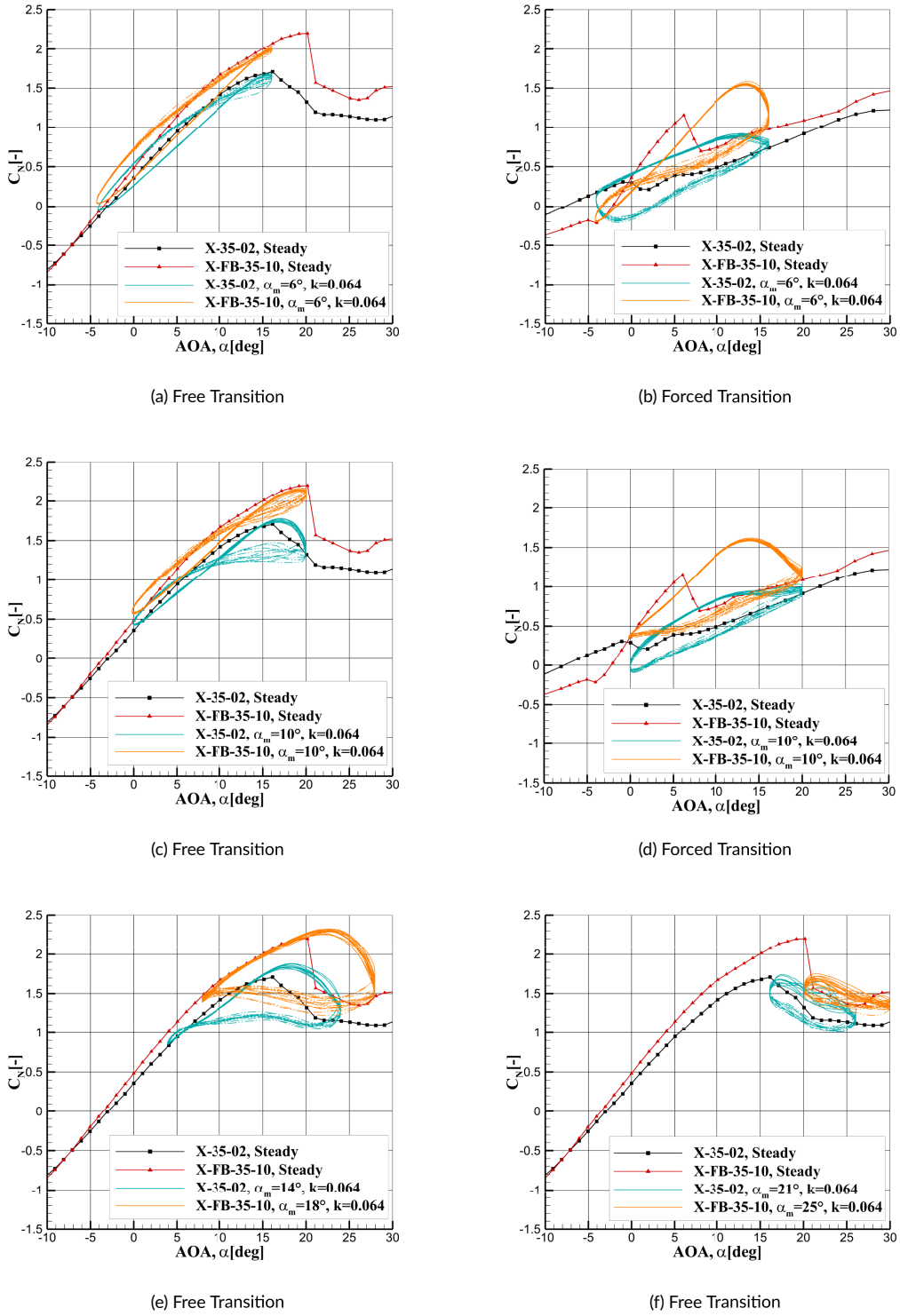

FIGURE 6 | Comparison between the static and dynamic polar curves for X-35-02 and X-FB-35-10 airfoils, in free and forced transition flow regimes [$Re = 1 \times 10^6$].

airfoil than the flatback airfoil. During the DS-phase, because of the pressure lag, the large separation bubble remains longer on the airfoil, and thus, the dynamic C_N drops below the static C_N. Since the separation bubble on the X-35-02 airfoil retracts faster than the flatback airfoil, the dynamic C_N increases from the one quarter of the DS-phase.

Figures 7 and 8 present the pressure distributions of the above polars at three different angles of attack of 1/4, 1/2, and 3/4 of the US- and DS-phases. Figures 7 and 8a–c represent the pressure distribution of Figure 6a case at the $\alpha_m = 6^\circ$. At 1° angle of attack, in the US-phase, there is no sign of flow separation at the trailing edge and the suction peak is lower than the static

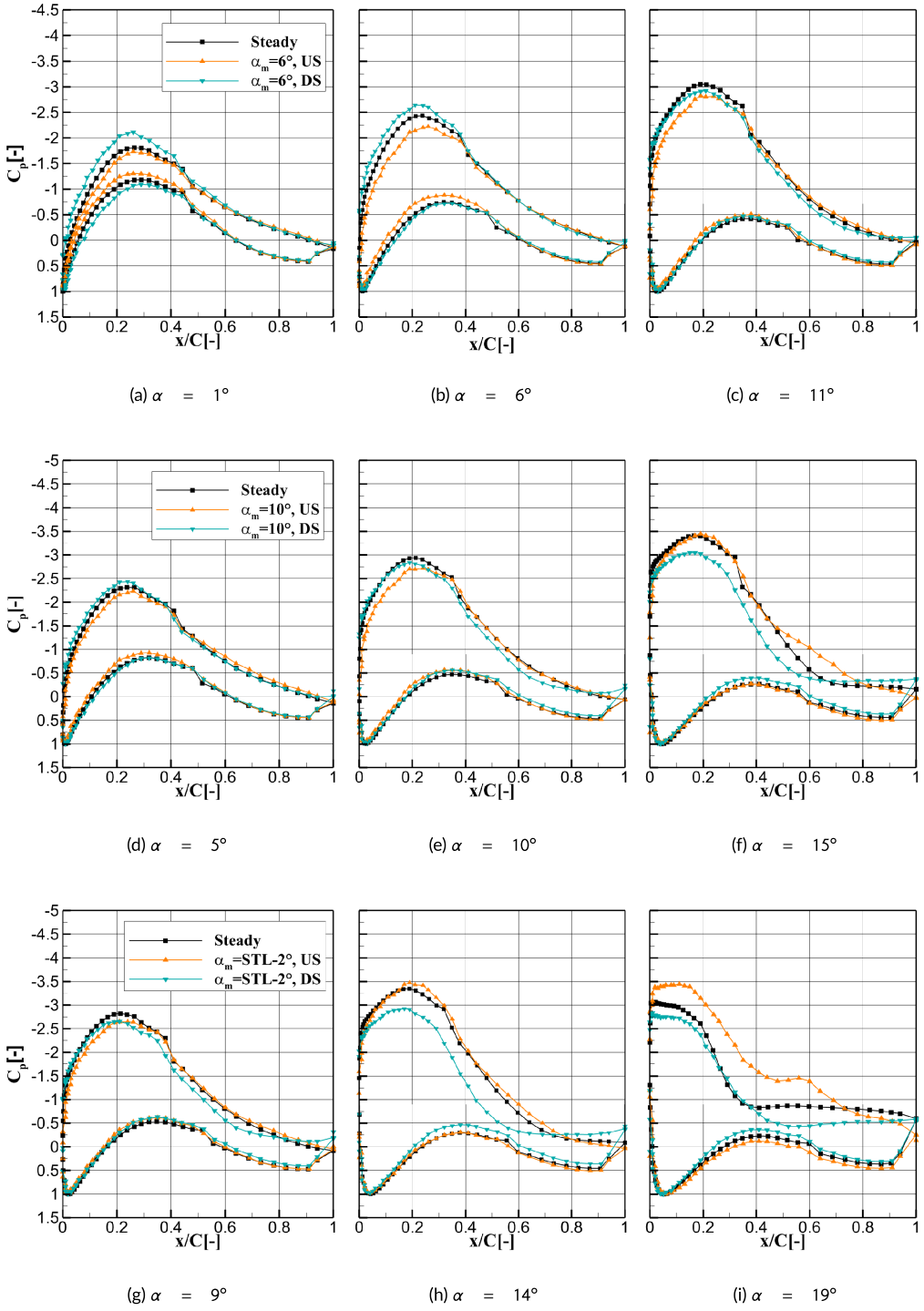

FIGURE 7 | Dynamic pressure coefficient comparison for X-35-02 airfoil, in free transition flow regime ($k = 0.064$, $Re = 1 \times 10^6$).

pressure distribution, because of the pressure adaptation lag and reduction of the relative velocity above the surface, due to the pitching of the airfoil. If the flow remains attached, the suction peak pressure reduction is also visible on the other US-phases figures. Looking at the US-phases, that is, figures (a) to (c), the suction peak pressure increases slowly with increasing the angle of attack. On the other hand, during the DS-phase, the maximum suction peak is higher than the static peak, improving the pressure gradient and flow stability for $\alpha = 1^{\circ}$ and $\alpha = 6^{\circ}$. This accounts for the higher dynamic normal force values observed during the downstroke (DS) phase compared to the steady polar. A short pressure plateau at $\alpha = 11^{\circ}$ near the trailing edge for the X-35-02 airfoil is related to the trailing edge separation.

With increasing the mean angle of attack to 10°, the X-FB-35-10 airfoil shows similar behavior as described above. Moreover, a flat suction peak plateau is formed at the beginning of the DS-phase. In contrast, the TSA of the X-35-02 airfoil surpasses the static stall angle of attack, resulting in a more pronounced

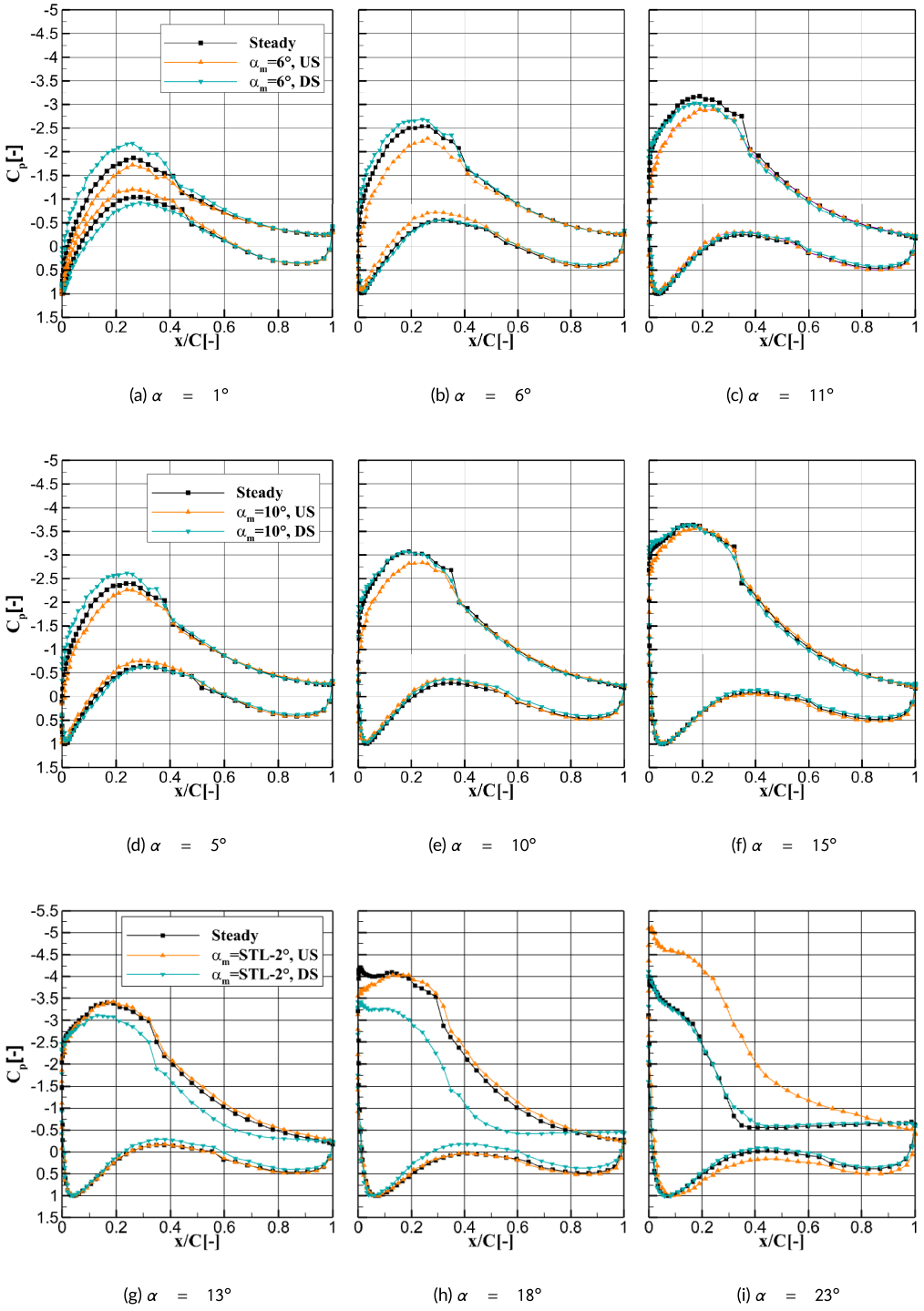

FIGURE 8 | Dynamic pressure coefficient comparison for X-FB-35-10 airfoil, in free transition flow regime ($k = 0.064$, $Re = 1 \times 10^6$).

dynamic stall compared to the X-FB-35-10 airfoil. Figures 7 and 8d–f show, as expected, a lower suction peak during the US-phase than the static pressure coefficient, except for the X-35-02 airfoil at $\alpha = 15^{\circ}$, where the dynamic C_N exceeds the steady value. In the DS-phase, the flow separation is visible on the suction side as a flat plateau before the trailing edge. This separation bubble becomes smaller with a decrease in the angle of attack. Moreover, the suction peak, formed as a plateau near the leading edge, becomes curved and moves towards the trailing edge.

At $\alpha_m = STL\text{-}2^{\circ}$, during the US-phase, the suction peak increases, moves towards the leading edge, and becomes wider with increasing the angle of attack as presented in Figures 7 and 8g–i. Note that the pressure gradient for the flatback airfoil is higher than that of the other airfoil. As previously described, the flow separation rapidly propagates from the trailing edge towards the leading edge of both airfoils due to the stagnation of the angle of attack at the end of the US-phase on one side and a very high pressure gradient on the other side. On the other hand, owing to the higher suction peak of the X-FB-35-10 airfoil during the

DS-phase, the flow reattachment process takes longer than the X-35-02 airfoil.

Figure 9a shows the impact of reduced frequency on the dynamic normal coefficient characteristics of the X-35-02 airfoil in the attached flow region of the normal force polar under free transition flow conditions. The results indicate a rise in pressure lag as the reduced frequency increases, leading to a decrease in the normal coefficient during the US-phase and an increase during the DS-phase within the attached flow region of the cycles. Moreover, the trailing edge separation, occurring at the TSA, persists longer above the airfoil surface compared to lower reduced frequencies. Additionally, the dynamic normal coefficient aligns with the static value only at a reduced frequency of $k = 0.032$, which escalates with increasing reduced frequency due to heightened pressure lag. Note that the MDNS and NFR are reduced with increasing the reduced frequency. The identical dynamic characteristics are observed on the X-FB-35-10 airfoil in the attached segment of the normal force polar, as depicted in Figure 9b.

As the mean angle of attack increases and the TSA surpassing the static stall angle of attack, the characteristics of the cycles are altered with an increase in reduced frequency. The increase in pressure adaptation lag and the delay in the development of the trailing edge separation bubble above the airfoil alter the characteristics of dynamic stall and the recovery shape. This cycle development is evident in Figure 10a. It is observed that dynamic stall recovery occurs at lower angles of attack as the reduced frequency increases due to higher pressure lag. Additionally, increasing the reduced frequency delays the onset of dynamic stall. With an increase in reduced frequency, the separation bubble at the TSA develops shorter above the airfoil compared to lower reduced frequencies. Thus, the dynamic C_N drops at higher angles of attack, compared to the lower reduced frequencies.

The effect of the reduced frequency on the dynamic stall characteristics of both airfoils at the mean angle of attack of $\alpha_m = STL\text{-}2^{\circ}$ is presented in Figures 10b and 11a. The results show that the maximum dynamic C_N overshoot increases, with increasing the reduced frequency. At high reduced frequencies, the pressure adaptation lag increases, leading to less development of the separation bubble above the airfoil compared to lower reduced frequencies during the US-phase. Thus, the flow remains attached to higher angles of attack, which leads to a higher C_N overshoot. It is visible from the mentioned figures that the dynamic stall occurs before the

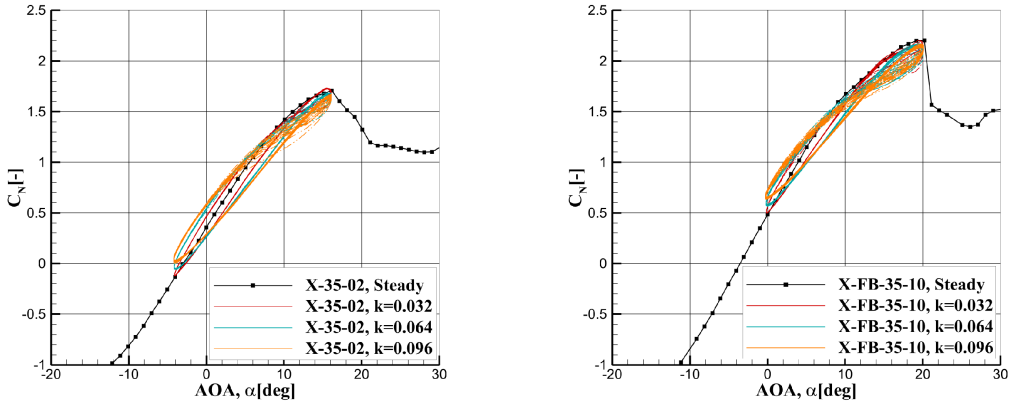

(a) α_m = 6° (b) α_m = 10°

FIGURE 9 | Effect of the reduced frequency on the normal coefficient, in free transition flow regime ($Re = 1 \times 10^6$).

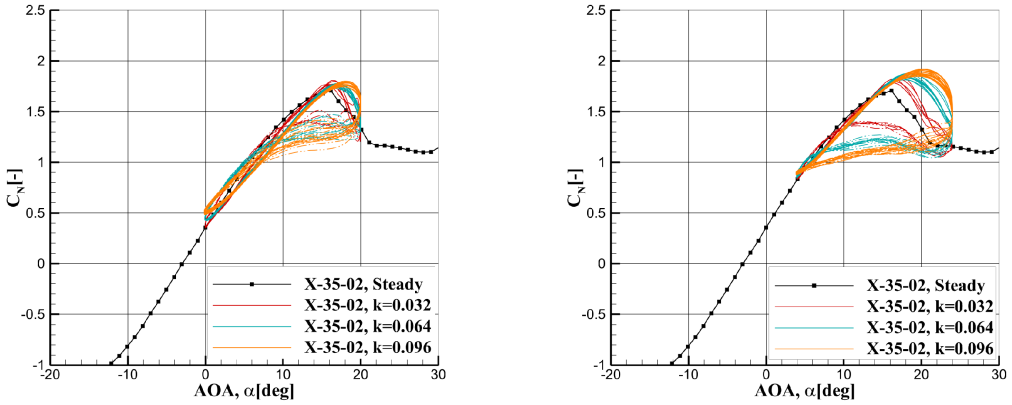

(a) α_m = 10° (b) α_m = 14°

FIGURE 10 | Effect of the reduced frequency on the normal coefficient of X-35-02 airfoil, in free transition flow regime ($Re = 1 \times 10^6$).

TSA and the dynamic stall angle of attack moves towards the TSA, with increasing the reduced frequency. At low reduced frequencies, the normal force coefficient drops to a similar order as the static curve after dynamic stall. As the reduced frequency increases, the normal coefficient exhibits less of a drop after the stall, which is attributed to the slower development of the trailing edge separation bubble above the airfoil due to increased pressure lag. In contrast to the dynamic loops in the linear part of the normal coefficient curve, the NFR and MDNS are increased with increasing the reduced frequency. Furthermore, the Flatback airfoil has a higher NFR and MDNS than the X-35-02 airfoil, due to a higher maximum dynamic C_N. Note the longer dynamic stall recovery of the flatback airfoil compared to the X-35-02 airfoil.

The same dynamic condition is shown for the X-FB-35-10 airfoil in the forced transition condition in Figure 11b. The normal coefficient drops to the static curve level of the static curve and tracks it at lower angles of attack. The same dynamic characteristics are seen with increasing the reduced frequency, that is, slower C_N drop after dynamic stall occurrence and higher dynamic stall angle of attack. Despite exceeding the static stall angle of attack, it is intriguing to observe that increasing the reduced frequency can effectively postpone the onset of dynamic stall. Note the effect of negative dynamic stall due to pressure-side separation at the end of the DS-phase.

Figure 12a,b shows the dynamic stall characteristics of both airfoils in the forced transition flow regime in the poststall region. The dynamic loops for the X-35-02 airfoil are close to the static normal curve. An increase in reduced frequency slightly raises the NFR and MDNS in the X-FB-35-10 airfoil, which is related to the not-fully-separated flow on the suction side of the airfoil at the beginning of the US-phase. Increasing the reduced frequency pulls this small, attached flow part above the airfoil to higher angles of attack. On the other hand, the X-35-02 airfoil reacts to the increase of reduced frequency differently, due to heavy flow separation above the airfoil. In this case, only the flat loops transform into small oval loops.

The dynamic stall characteristics of both airfoils in the poststall region and free transition flow regime are presented in Figure 13a,b. For the X-35-02 airfoil at a reduced frequency of $k = 0.032$, the normal coefficient exhibits a loop around the static curve. As the reduced frequency increases, the

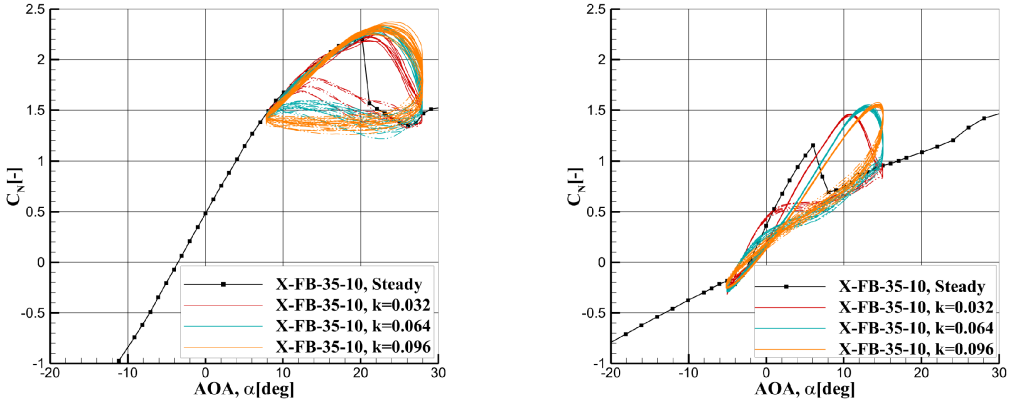

(a) α_m = 18°, Free Transition (b) α_m = 5°, Forced Transition

FIGURE 11 | Effect of the reduced frequency on the normal coefficient of X-FB-35-10 airfoil, in free and forced transition flow regime ($Re = 1 \times 10^6$).

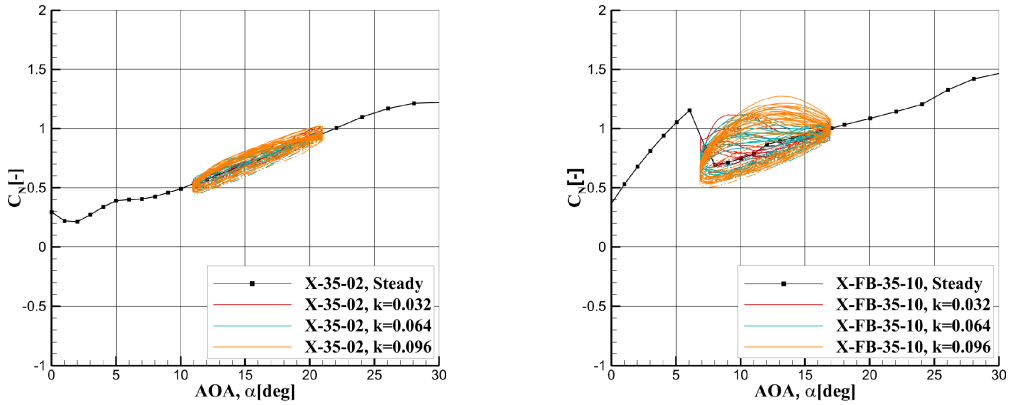

(a) α_m = 16° (b) α_m = 12°

FIGURE 12 | Effect of the reduced frequency on the poststall dynamic normal coefficient, in forced transition flow regime ($Re = 1 \times 10^6$).

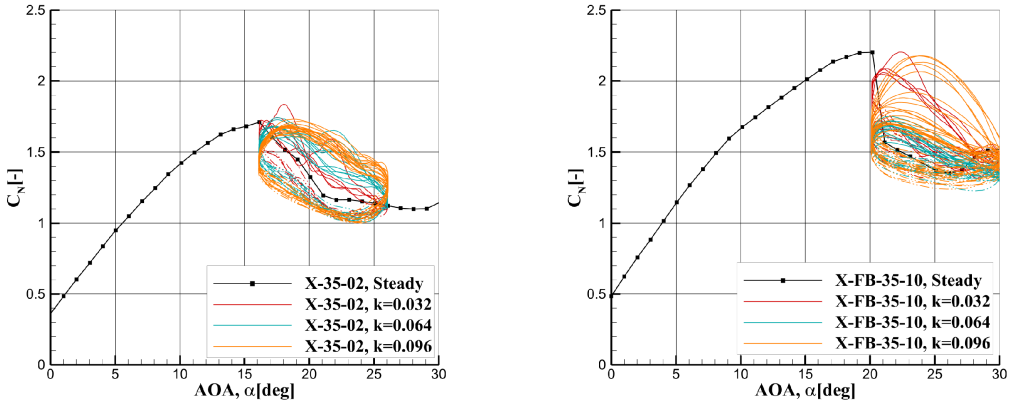

(a) $\alpha_m = 21°$ (b) $\alpha_m = 25°$

FIGURE 13 | Effect of the reduced frequency on the poststall dynamic normal coefficient, in free transition flow regime ($Re = 1 \times 10^6$).

cycles transform into a more oval shape, and the US-phases become more stable, which is related to the increase of pressure lag. However, due to the large separation bubble above the airfoil, the separation bubble size starts to increase during the US-phase. Note that these loops are clockwise. The separation bubble expansion starting point is detectable as the maximum normal coefficient in the US-phase. Note how this point moves to higher angles of attacks while increasing the reduced frequency. The reduced frequency does not affect the NFR; however, it only shifts the phase of extremum points. The MDNS decreases, with increasing the reduced frequency. Furthermore, the standard deviation of the normal coefficient in the loops decreases with increasing the reduced frequency.

The dynamic loops of the X-FB-35-10 airfoil vary due to the distinct static stall characteristics of this airfoil. At a reduced frequency of $k = 0.032$, the US-phase normal coefficient is higher than the static values but then drops back to static levels as a result of the separation bubble forming on the suction side. In contrast, the DS-phases closely follow the static curve due to a significant separation bubble in the poststall region. Increasing the reduced frequency to $k = 0.064$ leads to a reduction in the NFR. Notice the distinct patterns of the US-phases at $k = 0.096$, referred to as bifurcation flow. Due to the highly unstable flow conditions, different sizes of separation bubbles may form at the conclusion of the DS-phase during each cycle above the airfoil. Consequently, various configurations of the upstroke phase are possible depending on the pressure coefficient distribution on the suction side of the airfoil.

4 | Conclusion

The main goal of this investigation is to understand the difference in the dynamic stall characteristics of thick flatback and nonflatback wind turbine airfoils. The measurements are performed in the LTT wind tunnel of the TU Delft. Two different airfoils, X-35-02 and X-FB-35-10 flatback airfoil, are tested at different mean angles of attack, reduced frequencies, and in free and forced transition flow regimes. The surface pressure measurement method was used to determine the aerodynamic coefficients.

The steady measurements show a higher stall angle of attack, higher maximum lift coefficient, and lower sensitivity to the leading edge roughness for the X-FB-35-10 airfoil. Increasing the trailing edge thickness reduces the pressure gradients above the airfoil, stabilizing the boundary layer and increasing the airfoil's resistance to the adverse pressure gradient.

The dynamic measurements show that the X-FB-35-10 flatback airfoil has more stable dynamic loops, that is, fewer lift instabilities, higher lift overshoot, and higher MDNS than the X-35-02 airfoil in the attached flow part of the lift curve in both free and forced transition flow regimes, due to its better suction side pressure gradient characteristics. The stability of dynamic lift decreases with increasing reduced frequency in the presence of light trailing edge separation.

In the dynamic stall condition, the trailing edge separation bubble development over the flatback airfoil is slower compared to the sharp trailing edge airfoil, which delays the onset of the dynamic stall. Increasing the reduced frequency increases the pressure development lag on the suction side of the airfoil, leading to slower separation expansion and increased dynamic lift overshoot in both free and forced transition flow regimes. This flow stabilization is more pronounced for the flatback airfoil. For the same reason, the drop of the lift in the dynamic stall onset is reduced with increasing the reduced frequency. Abrupt or smooth steady stall characteristics affect the dynamic stall behavior, especially in the DS-phase. Hence, the flatback airfoil has more abrupt dynamic stall behavior at low reduced frequencies than the sharp trailing edge airfoil.

In the poststall conditions, due to the very high sensitivity of the X-35-02 airfoil to the leading edge roughness and large-size flow separation, the dynamic lift remains close to the static curve in the forced transition flow regime. Nevertheless, significant dynamic lift fluctuations are observed for the flatback airfoil in forced transition flow and under free transition conditions for both airfoils.

The findings of this research indicate that while the dynamic stall properties of flatback airfoils share similarities with those of nonflatback airfoils, there are also notable differences between the two. Using flatback airfoils in wind turbines has

been found to delay the onset of dynamic stall, which can have a significant impact on turbine operation. This delay in stall onset reduces the turbine's sensitivity to wind fluctuations and prevents vortex-induced vibrations of the rotor blade during high turbulence conditions, ultimately improving the overall efficiency and reliability of the turbine. Consequently, the utilization of flatback airfoils in wind turbine blades has been discovered to enhance the structural and steady aerodynamic properties. However, additional research is necessary to fully understand their potential for improving the dynamic loads of the rotor blade.

Nomenclature

α	angle of attack (°)
α_0	speed of sound (∘)
α_j	shear wave number (–)
α_m	mean angle of attack (°)
γ	specific heat ratio (–)
μ	absolute viscosity ($\mathrm{Ns/m^2}$)
ν	frequency (Hz)
ρ_s	mean density ($\mathrm{kg/m^3}$)
σ	diaphragm volume increase (–)
A	amplitude of oscillation (°)
AOA	angle of attack (°)
C	chord (m)
C_L	lift coefficient (–)
C_D	drag coefficient (–)
C_M	moment coefficient (–)
C_N	normal coefficient (–)
C_p	pressure coefficient (–)
DS	down-stroke (–)
ETM	extreme turbulence model (–)
FFT	Fast Fourier Transformation (–)
i	imaginary number (–)
J_n	Bessel function (–)
k	reduced frequency (–)
k_p	polytropic constant (–)
L	tube length (m)
$MDNS$	mean dynamic normal slope (Rad)
NTM	normal turbulence model (–)
NFR	normal force range (–), the distance between maximum and minimum C_N
P_r	Prandtl number (–)
R	tube radius (m)
STL	stall (–)
t	time (s)
TSA	top stagnation angle (°)
BSA	bottom stagnation angle (°)
US	up-stroke (–)
v	pressure transducer volume ($\mathrm{m^3}$)
V_{in}	Cut-in velocity (m/s)
V_{out}	Cut-out velocity (m/s)
V_r	Rated velocity (m/s)
V_t	tube volume ($\mathrm{m^3}$)
V_v	pressure transducer volume ($\mathrm{m^3}$)

Acknowledgments

This work was funded by the Nordex Energy SE & Co. KG, and the authors are very grateful for this support.

Data Availability Statement

The data that support the findings of this study are available from the corresponding author upon reasonable request.

Peer Review

The peer review history for this article is available at https://www.webofscience.com/api/gateway/wos/peer-review/10.1002/we.70061.

References

1. M. I. Blanco, "The Economics of Wind Energy," *Renewable and Sustainable Energy Reviews* 13, no. 6–7 (2009): 1372–1382, https://doi.org/10.1016/j.rser.2008.09.004.

2. T. D. Ashwill, "Parametric Study for Large Wind Turbine Blades. SAND2002–2519," (2002), https://doi.org/10.2172/801402.

3. T. D. Ashwill, "Cost Study for Large Wind Turbine Blades. SAND2003–1428," (2003), https://doi.org/10.2172/811158.

4. L. Wang, X. Liu, and A. Kolios, "State of the Art in the Aeroelasticity of Wind Turbine Blades: Aeroelastic Modelling," *Renewable and Sustainable Energy Reviews* 64 (2016): 195–210, https://doi.org/10.1016/j.rser.2016.06.007.

5. H. Snel, "Review of Aerodynamics for Wind Turbines," *Wind Energy* 6, no. 3 (2003): 203–211, https://doi.org/10.1002/we.97.

6. G. Leishman, "Challenges in Modelling the Unsteady Aerodynamics of Wind Turbines," *Wind Energy* 5 (2002): 85–132, https://doi.org/10.1002/we.62.

7. M. A. Khan, "Dynamic Stall Modeling for Wind Turbines. Master Thesis TU Delft Aerospace Engineering," (2018), http://resolver.tudelft.nl/uuid:f1ee9368-ca44-47ca-abe2-b816f64a564f.

8. M. M. Hand, D. A. Simms, L. J. Fingersh, D. W. Jager, and J. R. Cotrell, "Aerodynamics Experiment Phase V: Test Configuration and Available Data Campaigns. Technical Report, NREL/TP-500-29491," (2001), https://doi.org/10.2172/787980.

9. G. Leishman, *Principles of Helicopter Aerodynamics*, 2nd ed. 0521858607 (Cambridge University Press, 2006).

10. R. Pereira, G. Schepers, and M. Pavel, "Validation of the Beddoes-Leishman Dynamic Stall Model for Horizontal Axis Wind Turbines Using Mexico Data," *Wind Energy* 16, no. 2 (2013): 207–219, https://doi.org/10.1002/we.541.

11. M. Kramer, "Increase in the Maximum Lift of an Airplane Wing due to Sudden Increase in Its Effective Angle of Attack Resulting From a Gust," National Advisory Committee for Aeronautics 1932;(TM 678).

12. L. E. Ericsson, "Comments on Unsteady Airfoil Stall," *Journal of Aircraft* 4, no. 5 (1967): 478–480.

13. F. O. Carta, "Effect of Unsteady Pressure Gradient Reduction on Dynamic Stall Delay," *Journal of Aircraft* 8, no. 10 (1971): 839–840.

14. W. Johnson and N. D. Ham, "On the Mechanism of Dynamic Stall," *Journal of the American Helicopter Society* 17, no. 4 (1972): 36–45.

15. L. E. Ericsson and J. P. Reding, "Dynamic Stall of Helicopter Blades," *Journal of the American Helicopter Society* 17, no. 1 (1972): 11–19.

16. W. McCroskey, "Inviscid Flowfield of an Unsteady Airfoil," *AIAA Journal* 11 (1973): 1130–1137, https://doi.org/10.2514/6.1972-681.

17. T. S. Beddoes, "Representation of Airfoil Behaviour," *Vertica* 7, no. 2 (1983): 183–197.

18. K. W. McAlister and L. W. Carr, "Water Tunnel Visualizations of Dynamic Stall," *Journal of Fluids Engineering* 101 (1979): 376–380.

19. R. M. Scruggs, J. F. Nash, and R. E. Singleton, "Analysis of Flow-Reversal Delay for a Pitching Airfoil," AIAA 12th Aerospace Sciences Meeting, (1974): 74–183, https://doi.org/10.2514/6.1974-183.

20. D. P. Telionis, "Calculation of Time Dependent Boundary Layers," Unsteady Aerodynamics Proc Symp Univ Arizona, (1975): 155.

21. W. J. McCroskey, "Some Current Research in Unsteady Fluid Dynamics ASME Freeman Scholar Lecture," *Journal of Fluids Engineering, Transactions of the ASME* 99 (1975): 8–38.

22. N. D. Ham, "Aerodynamic Loading on a 2 - D Airfoil During Dynamic Stall," *AIAA Journal* 6, no. 10 (1968): 1927–1934, https://doi.org/10.2514/3.4902.

23. W. J. McCroskey, "Recent Developments in Rotor Blade Stall," AGARD CP (111) (1972).

24. W. J. McCroskey and R. Fisher, "Dynamic Stall of Airfoils and Helicopter Rotors," AGARD Paper, (1972):595.

25. T. S. Beddoes, "A Qualitative Discussion of Dynamic Stall. AGARD Report (679)," (1979).

26. T. S. Beddoes, "Onset of Leading Edge Separation Effects Under Dynamic Conditions and Low Mach Number. Proceedings of the 34th Annual Forum of the American Helicopter Society,"(1978).

27. P. F. Lorber, "Compressibility Effects on the Dynamic Stall of a Three-Dimensional Wing. AIAA 92–0191, 30th Aerospace Sciences Meeting," (1992), https://doi.org/10.2514/6.1992-191.

28. M. S. Chandrasekhara and L. W. Carr, "Compressibility Effects on Dynamic Stall of Oscillation Airfoil," AGARD, (1994):CP-552.

29. J. Liiva, F. J. Davenport, L. Gray, and I. C. Walton, "2 - D Tests of Airfoils Oscillating Near Stall. USAAVLABS 1968;(TR 68–13, Vols. I II),".

30. M. E. Wood, "Results of Oscillatory Pitch and Ramp Tests on the NACA 0012 Blade Section," Aircraft Research Association, Bedford, UK, ARA 1979;(Memo 220).

31. T. S. Beddoes, "A Synthesis of Unsteady Aerodynamic Effects Including Stall Hysteresis," *Vertica* 1, no. 2 (1976): 113–123.

32. R. A. M. Galbraith, A. J. Niven, and L. Y. Seto, "On the Duration of Low Speed Dynamic Stall. 15th Congress of the International Council of the Aeronautical Sciences," (1986): 522–531.

33. R. B. Green and R. A. M. Galbraith, "Dynamic Recovery to Fully Attached Aerofoil Flow From Deep Stall," *AIAA Journal* 33, no. 8 (1995): 1433–1440.

34. M. Doosttalab and O. Frommann, "Multidisciplinary Design and Verification of the HB Flatback Airfoil Family," *AIAA Journal* 57, no. 11 (2019): 4639–4649, https://doi.org/10.2514/1.J057684.

35. Delft University of Technology, "Low Turbulence Tunnel (LTT),".

36. Biao LUaMB, "Experimental Investigation of the Wake Survey Method for a Bluff Body With Highly Turbulent Wake," AIAA (2002):(2002–3060), https://doi.org/10.2514/6.2002-3060.

37. C. Dalton, "Allen and Vincenti Blockage Corrections in a Wind Tunnel," No. vol. 9, no. 9, (1971), https://doi.org/10.2514/3.6435.

38. H. B. H. Tijdeman, "Theoretical and Experimental Results for the Dynamic Response of Pressure Measuring Systems. Report 1965;(NLR-TR F.238)," (1965).

Appendix A

Bergh and Tijdeman [38] concluded that varying the frequency of constant fluctuations for a given pressure measurement system with a constant pressure input results in the system's frequency response. Having the frequency response of a system makes it possible to calculate the system's time response to any random input signal. This theory decomposes a pressure measurement system into an N subsection, in which the input pressure of a section is the output pressure of the N-1 section. The pressure transfer function for a single pressure measurement system, that is, for every subsystem, is given by the following:

$$\frac{p_1}{p_0} = \left[cosh\langle\varphi L\rangle + \frac{V_v}{V_t}\left(\sigma + \frac{1}{k}\right)n\varphi L sinh\langle\varphi L\rangle\right]^{-1} \tag{1}$$

$$\varphi = \frac{\nu}{\alpha_0}\sqrt{\frac{J_0\langle\alpha\rangle}{J_2\langle\alpha\rangle}}\sqrt{\frac{\gamma}{n}} \tag{2}$$

$$\alpha = i\sqrt{iR}\sqrt{\frac{\rho_s \upsilon}{\mu}} \tag{3}$$

$$n = \left(1 + \frac{\gamma - 1}{\gamma}\frac{J_2\left\langle\alpha\sqrt{P_r}\right\rangle}{J_0\left\langle\alpha\sqrt{P_r}\right\rangle}\right)^{-1} \tag{4}$$

Here, V_v is the pressure transducer volume, V_t is the tube volume, R is the tube radius, L is the length of the tube, i is the imaginary number, J_n is the Bessel function of the first kind of order n, k is the polytropic constant for the volumes, and α_0 is the speed of sound. ρ_s is the mean density, α is the shear wave number, μ is the absolute fluid viscosity, γ is the specific heat ratio, ν is the frequency. υ is the pressure transducer volume, and P_r is the Prandtl number. σ is the dimensionless volume increase in the pressure transducer due to diaphragm deflection. For several pressure tubes, which are connected in series,

$$\frac{p_N}{p_0} = \frac{p_N}{p_{N-1}} \cdots \frac{p_1}{p_0} \tag{5}$$

Defining the relation between each subsystem, a square step response along with fast Fourier transformation (*FFT*) and inverse *FFT* is used to predict the domain frequency response of the system [36]. Figure A1 shows the difference between the measured uncorrected pressure and corrected pressure for the phase delay and amplitude on one pressure tap near the trailing edge at the suction side of the X-35-02 airfoil. Since the connection characteristics, including tube length, cavities, and potential adaptors between the pressure sensors and the pressure coupling connection within the pressure acquisition system, are unknown, a CFD simulation at 1 Hz was utilized in the linear region of the lift polar to determine the equivalent tube length and diameter of the unidentified components, ultimately validating the pressure correction method.

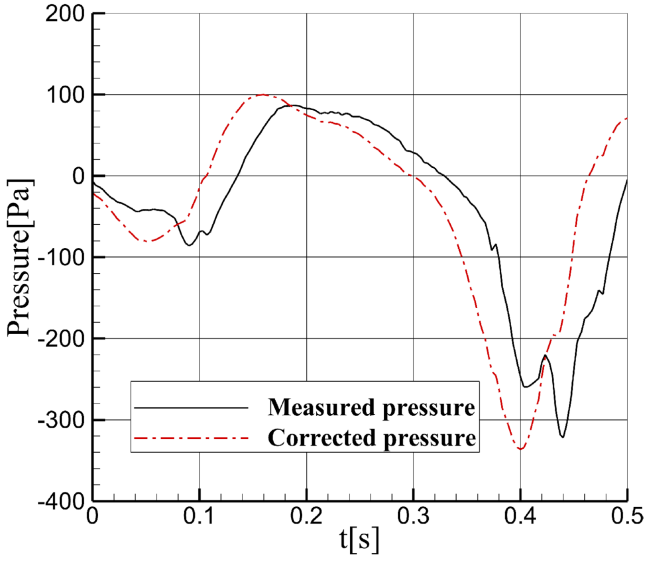

FIGURE A1 | Comparison between the measured and the corrected data of a pressure tap of X-35-02 airfoil ($Re = 1 \times 10^6$).